

Direct Visualization of Gigahertz Acoustic Wave Propagation in Suspended Phononic Circuits

Daehun Lee^{1,‡}, Qiyu Liu,^{2,‡} Lu Zheng,¹ Xuejian Ma,¹ Huan Li,² Mo Li,^{2,3,*} and Keji Lai^{1,†}

¹*Department of Physics, University of Texas at Austin, Austin, Texas 78712, USA*

²*Department of Electrical and Computer Engineering, University of Washington, Seattle, Washington, 98195, USA*

³*Department of Physics, University of Washington, Seattle, Washington, 98195, USA*



(Received 26 May 2021; revised 4 August 2021; accepted 31 August 2021; published 28 September 2021)

We report direct visualization of gigahertz-frequency Lamb-wave propagation in aluminum nitride phononic circuits by transmission-mode microwave impedance microscopy (TMIM). Consistent with finite-element modeling, the acoustic eigenmodes in both a horn-shaped coupler and a subwavelength waveguide are revealed in the TMIM images. Using fast Fourier-transform filtering, we quantitatively analyze the acoustic loss of individual Lamb modes along the waveguide and the power-coupling coefficient between the waveguide and the parabolic couplers. Our work provides insightful information on the propagation, mode conversion, and attenuation of acoustic waves in piezoelectric nanostructures, which is highly desirable for designing and optimizing phononic devices for microwave-signal processing and quantum-information transduction.

DOI: 10.1103/PhysRevApplied.16.034047

I. INTRODUCTION

Acoustic waves in the radio-frequency (MHz to GHz) range propagate in solid structures with a speed of several km/s, which is 5 orders of magnitude slower than the speed of light. Therefore, transduction from electromagnetic waves to acoustic waves enables signal processing on a dramatically slower timescale and much reduced device dimensions. Because acoustic waves cannot propagate in a vacuum, radiative crosstalk between signal channels in acoustic devices is also much lower than in electromagnetic devices. As a result, various types of acoustic devices, such as surface acoustic wave, bulk acoustic wave, and flexural plate wave devices, are widely utilized as delay lines; filters; oscillators; convolvers in wireless-communication applications [1–3]; and mass, pressure, and flow sensors in sensing applications [4]. Recently, propagating acoustic waves are considered universal quantum interconnects between different solid-state qubit systems, e.g., defect centers and superconducting qubits [5–10], for two reasons. First, the quantum states of these systems are highly susceptible to mechanical deformation with high coupling coefficients [11–15]; second, the acoustic wave can propagate with very low loss and noise at low temperatures [16,17]. There is also strong interest in achieving efficient transduction between optical

and microwave photons mediated by acoustic modes in optomechanical systems through acousto-optic coupling [18]. Optical waves and microwave-frequency acoustic (or phononic) modes are confined in wavelength-scale structures and interact through efficient acousto-optic coupling [19–26]. However, direct conversion from optical photons to acoustic phonons is intrinsically low in energy efficiency because of their large disparity in frequency (approximately 5 orders of magnitude), assuming the same wavelengths. In contrast, converting MHz-to-GHz electromagnetic waves to acoustic phonons can be achieved much more efficiently using electromechanical transducers on piezoelectric materials [27–29]. To achieve efficient transduction, it is critical to engineer phononic structures to effectively guide and couple acoustic phonons into optomechanical systems.

A major challenge for designing phononic systems is that the density of state of acoustic phonons is very high [30], and different polarization modes inherently couple with each other through geometric deformation. With a high acoustic frequency, the ratio between the phononic structures' dimensions and the acoustic wavelength becomes high, making it computationally expensive to perform a full three-dimensional (3D) finite-element simulation. The mechanical properties of materials that are deposited during device fabrication are also more susceptible to fabrication processes than their optical properties, making simulations less accurate. To complement mechanical simulations, experimental probing of the acoustic fields has become an important field of research in recent

*moli96@uw.edu

†kejilai@physics.utexas.edu

‡These authors contributed equally to this work.

years. For instance, MHz surface displacement fields are imaged by scanning laser reflectometry [31,32], the pump-probe technique [33,34], homodyne and heterodyne interferometry [35–37], stroboscopic x-ray imaging [38,39], scanning electron microscopy (SEM) [40,41], scanning tunneling microscopy (STM) [42,43], and nonlinear acoustic force microscopy (AFM) [44]. However, none of these techniques can simultaneously achieve sub-100-nm spatial resolution and >1-GHz operation frequency, which are crucial for wavelength-scale acousto-optic devices. Thus, a method that allows nanoscale investigation of wave phenomena, such as interference, diffraction, and localization, of GHz acoustic waves is desirable for designing and optimizing efficient optomechanical systems.

Here, we report the visualization of 3.44-GHz Lamb waves in suspended aluminum nitride (AlN) phononic waveguides by transmission-mode microwave impedance microscopy (TMIM) [45,46]. The imaging results vividly demonstrate the coupling from antisymmetrical membrane modes to waveguide modes through a parabolic horn-shaped coupler. Using fast Fourier-transform (FFT) filtering, we identify individual waveguide modes and analyze their propagation loss along the waveguide. Our work provides insightful information on the propagation, attenuation, and coupling of Lamb waves in phononic circuits, which cannot be obtained by traditional microwave network analysis.

II. DEVICE AND SIMULATION

The suspended phononic circuits in this work are fabricated on *c*-axis polycrystalline AlN thin films (thickness

$t = 330$ nm) grown by magnetron sputtering on SiO_2/Si wafers. The circuit consists of an acoustic waveguide, with width $w = 1 \mu\text{m}$ and length $L = 100 \mu\text{m}$, connected to two identical parabolic horn-shaped acoustic couplers [47,48] with a length of $L_h = 100 \mu\text{m}$. The couplers are designed to focus acoustic waves to the waveguide from two interdigital transducers (IDTs), one used as a transmitter and one as a receiver. The waveguide and couplers are patterned by standard electron beam lithography (EBL) and plasma etching of AlN, using 240-nm-thick SiO_2 as the hard mask. The IDT fingers have an aperture width of $A = 20 \mu\text{m}$. They are fabricated by EBL with the deposition of 7-nm Cr and 100-nm Au, followed by a standard lift-off process. To reduce the acoustic loss due to internal reflection and destructive interference in the IDT region, we use the split-finger design with a period of $3 \mu\text{m}$ and four fingers per period [inset of Fig. 1(a)]. The third-harmonic mode with $\lambda = 1 \mu\text{m}$ excited by this IDT is the Lamb wave that is investigated below. Another layer of 7-nm Cr/300-nm Au is deposited to thicken the bonding pads. Finally, the 3- μm thermal SiO_2 underneath the AlN film is removed using a vapor HF etcher to release the device from the substrate.

Electrical characterization of the AlN phononic circuit is carried out with a vector network analyzer (VNA). The transmitter and receiver IDTs are connected to the VNA through microwave cables and a pair of rf probes. The measured reflection coefficient (S_{11}) spectrum [Fig. 1(b)] shows a resonance at $f = 3.44$ GHz, which corresponds to the excitation of the Lamb mode at $\lambda = 1 \mu\text{m}$. The transmission coefficient (S_{21}) spectrum [Fig. 1(c)] between the two IDTs shows a smaller peak at the same frequency, indicating transmission of the Lamb wave through the

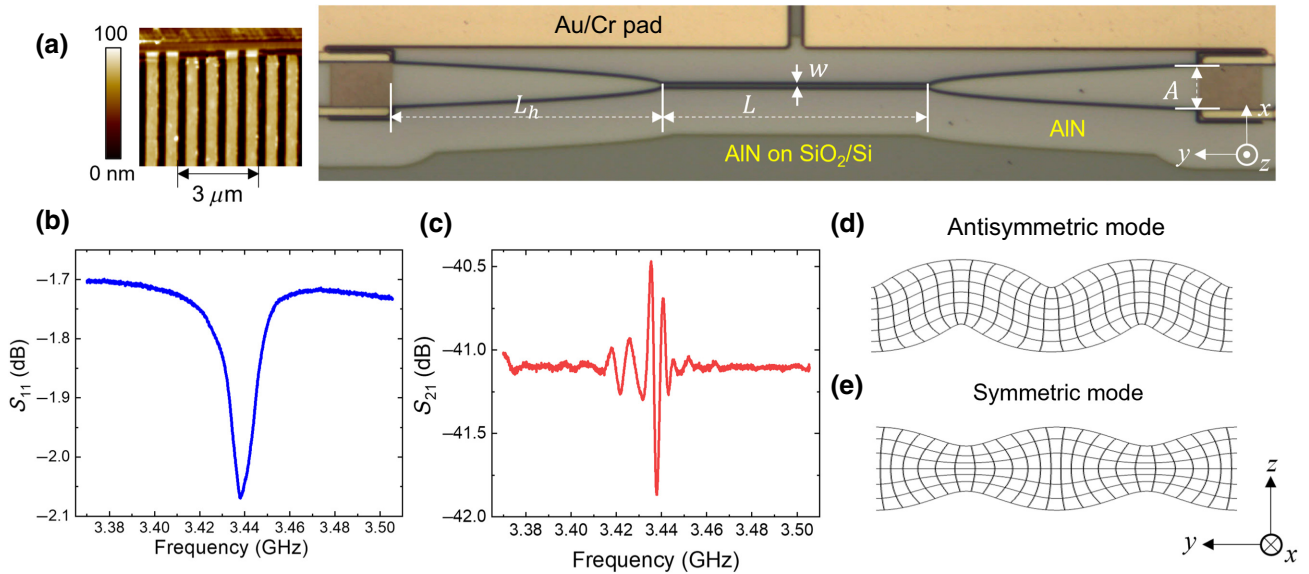


FIG. 1. (a) Optical image of the AlN phononic circuits. Inset on the left shows an AFM image of the split-finger IDT. (b) S_{11} and (c) S_{21} spectra of the device measured by a VNA, showing the acoustic resonance at $f = 3.44$ GHz. (d) Simulation results plotted in deformed grids showing the antisymmetric (A) and (e) symmetric (S) modes of the free-standing membrane at the IDT region.

circuit. Note that the S_{21} spectrum shows a few ripples, which can be attributed to the reflection and interference of the acoustic wave and the rf crosstalk between the input and output IDT ports. The capacitive crosstalk background signal is subtracted for clarity.

To understand the excited Lamb mode, we model the IDT region as a large AlN membrane and simulate with the finite-element method (FEM). Figures 1(d) and 1(e) show the simulated fundamental modes plotted in deformed grids, where the displacement fields are either A or S modes with respect to the x - y plane. Because the IDTs are patterned only on the top surface of the membrane, the electric fields generated by the IDTs are asymmetric along the thickness of the membrane. Consequently, the antisymmetric membrane modes are predominantly excited. Therefore, the observed resonance at 3.44 GHz is attributed to the antisymmetric Lamb mode, which agrees with the simulation results.

Compared with the membrane modes discussed above, which are only confined in the z direction, the acoustic wave propagating in suspended AlN circuits is also confined in the transverse x direction. In the following, we will denote the Lamb modes in the subwavelength waveguide as waveguide modes. Figure 2(a) shows the simulated dispersion relationship of various modes on a waveguide with a width of 1 μm and a thickness of 330 nm. The dashed line denotes the excitation frequency at 3.44 GHz, which intersects with three branches of dispersion curves of the

waveguide modes, hereafter labeled as $S0$, $A1$, and $A0$, respectively. Due to symmetry matching, the antisymmetric membrane mode excited by the IDTs can only couple to the $A0$ and $A1$ modes. Figures 2(b) and 2(c) display the simulated displacement fields of the two antisymmetric modes ($A0$ and $A1$). Here, the $A0$ mode in the lowest acoustic branch is the fundamental antisymmetric breathing mode with $\lambda = 1 \mu\text{m}$, where the displacement field is uniformly distributed in the cross section (x - z plane). $A1$ with $\lambda = 2 \mu\text{m}$ is the first-order antisymmetric mode, where the displacement is out of phase between the center of the waveguide and the boundary of the waveguide. Detailed simulation results of the $A0$, $S0$, and $A1$ modes are included in Appendix A.

III. EXPERIMENTAL RESULTS

Imaging of Lamb waves on the phononic circuit is carried out in our TMIM setup, an AFM-based technique with sub-100-nm spatial resolution [45,46]. Figure 3(a) shows the configuration of the TMIM experiment, where the acoustic wave is launched by the emitter IDT and the induced surface-potential modulation at GHz is detected by the tip. The signal is then amplified and demodulated by an in-phase-quadrature (I/Q) mixer, using the same microwave source as the reference signal. The time-varying acoustic signal is thus converted into

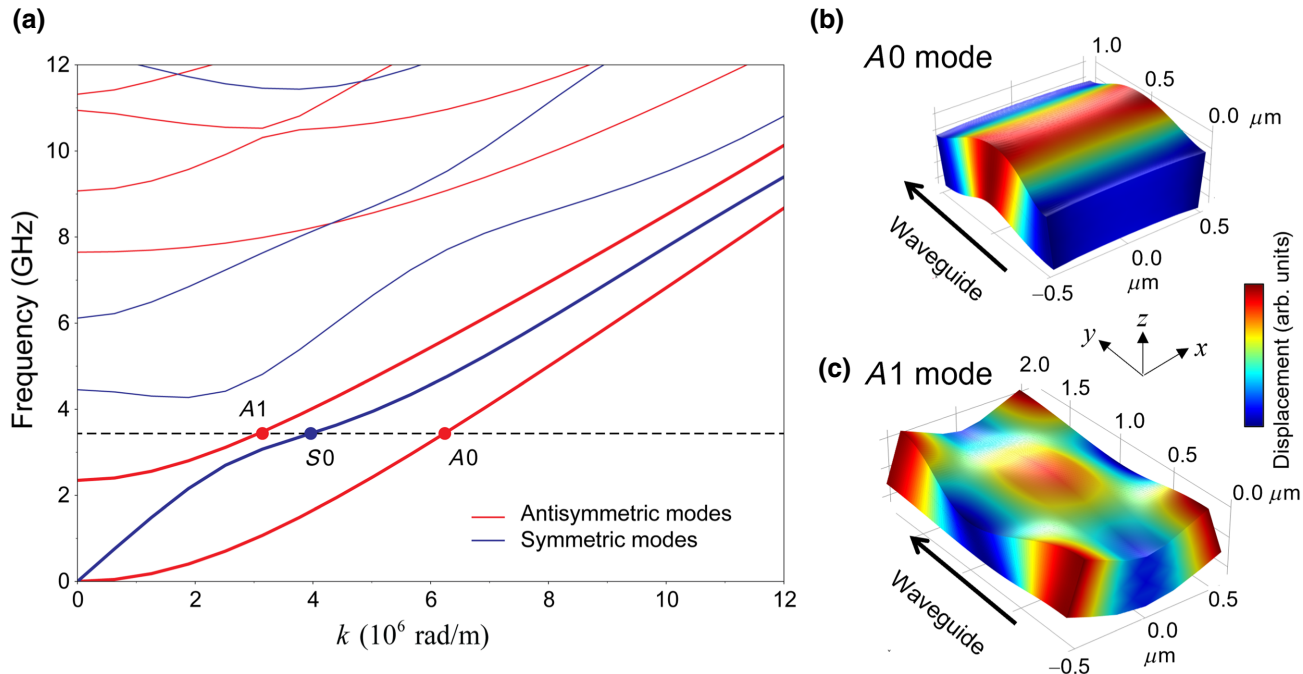


FIG. 2. (a) Calculated dispersion relationship of a free-standing AlN phononic waveguide of 1 μm wide. Red and blue curves represent antisymmetric and symmetric modes, respectively. Intersection points between the dashed line at $f = 3.44$ GHz and three lowest branches of the dispersion curves are labeled as $A0$, $S0$, and $A1$ (see text). (b) 3D simulation results showing the mode shape of $A0$ and (c) $A1$ modes with colors indicating the displacement magnitude.

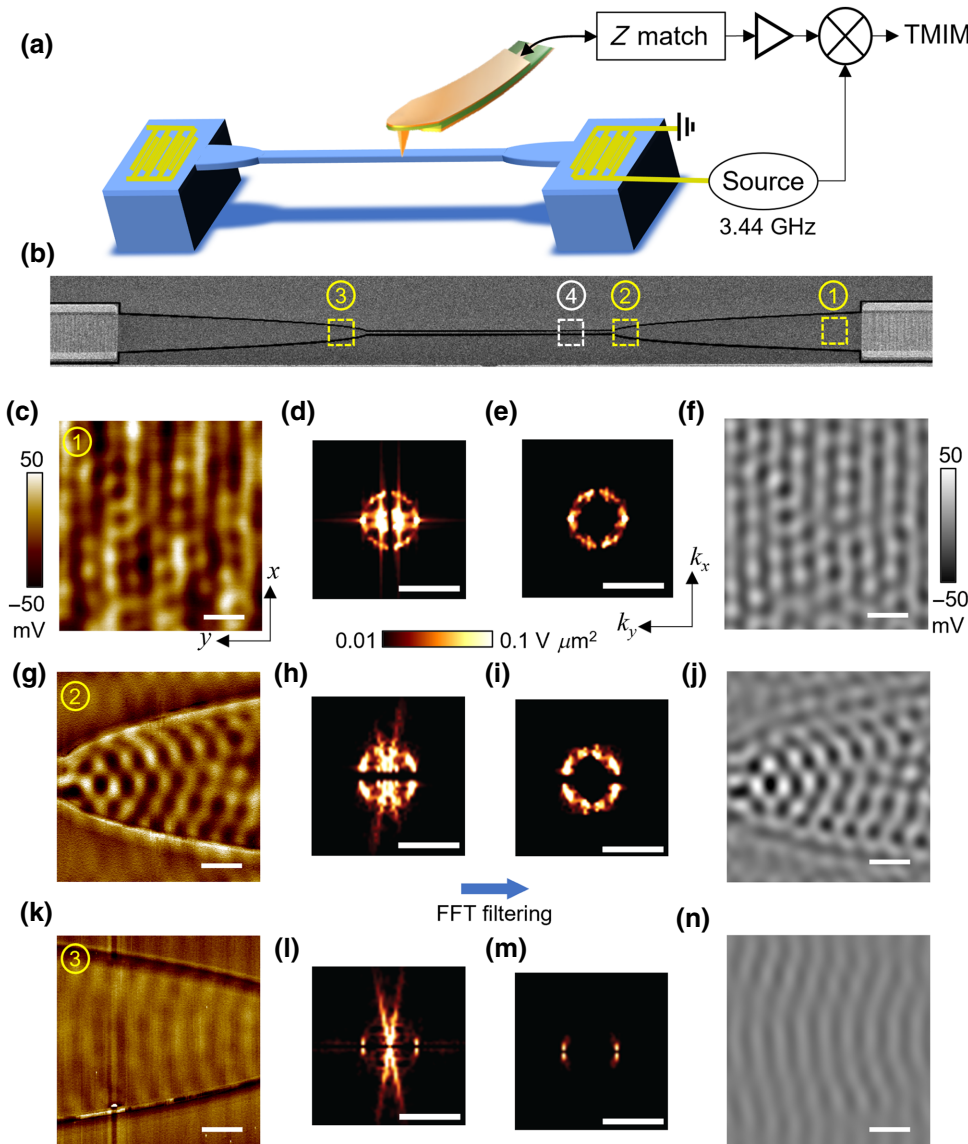


FIG. 3. (a) Schematics of the suspended phononic circuit and the TMIM setup. (b) SEM image of the device. Four dashed boxes show the locations where TMIM images are acquired. (c) TMIM image and (d) 2D FFT spectral image in box 1. (e) FFT image after removing the diffusive spots at the center. (f) Inverse FFT image of (e). (g)–(j) Same as (c)–(e) in box 2. (k)–(n) Same as (c)–(e) in box 3. Scale bars are $2 \mu\text{m}$ for real-space images and $2\pi \times 2 \mu\text{m}^{-1}$ for k -space FFT images. False-color scales for panels (c),(g),(k) are the same, so are (d),(e),(h),(i),(l),(m) and (f),(j),(n).

time-independent TMIM images, which are simultaneously acquired as the topographic image during scanning (Appendix B). For simplicity, we will present only one of the two orthogonal TMIM channels in the following discussion.

Figure 3(b) shows the SEM image of the AlN phononic circuit, where TMIM images are taken in several $10 \times 10 \mu\text{m}^2$ areas marked by dashed boxes. Near the emitter IDT, the acoustic pattern in Fig. 3(c) contains a substantial portion of left-moving waves. The corresponding 2D FFT spectral image is shown in Fig. 3(d). The large diffusive spots near the center of FFT data correspond to slow-varying background signals in the real space, presumably due to incoherent motion of the membrane. By filtering out this feature [Fig. 3(e)], one can see that the highest FFT intensity lies along the propagation direction (y axis) with a wavevector $|k| = 2\pi \times 1 \mu\text{m}^{-1}$, consistent

with $\lambda = 2\pi/k = 1 \mu\text{m}$ of the antisymmetric membrane mode. From the inverse FFT image in Fig. 3(f), it is nevertheless obvious that Lamb waves with the same $|k|$ along other in-plane directions are present because of multiple reflections from boundaries of the parabolic coupler. At the bottom of this parabola [Fig. 3(g)], the wave front is strongly curved. Correspondingly, while the Lamb wave retains the wavevector $|k| = 2\pi \times 1 \mu\text{m}^{-1}$, the FFT intensity in the y direction drops to zero [Fig. 3(h)]. Finally, in the other parabolic coupler near the exit side of the waveguide, a Lamb wave with the same $|k|$ but a much weaker amplitude is observed, as evidenced from both raw and FFT-filtered TMIM images [Figs. 3(k)–3(n)].

We now focus our attention on acoustic modes in the suspended phononic waveguide and compare the results with the FEM simulation in Fig. 2. Figure 4(a) shows the TMIM image taken in box 4, where a complex waveform

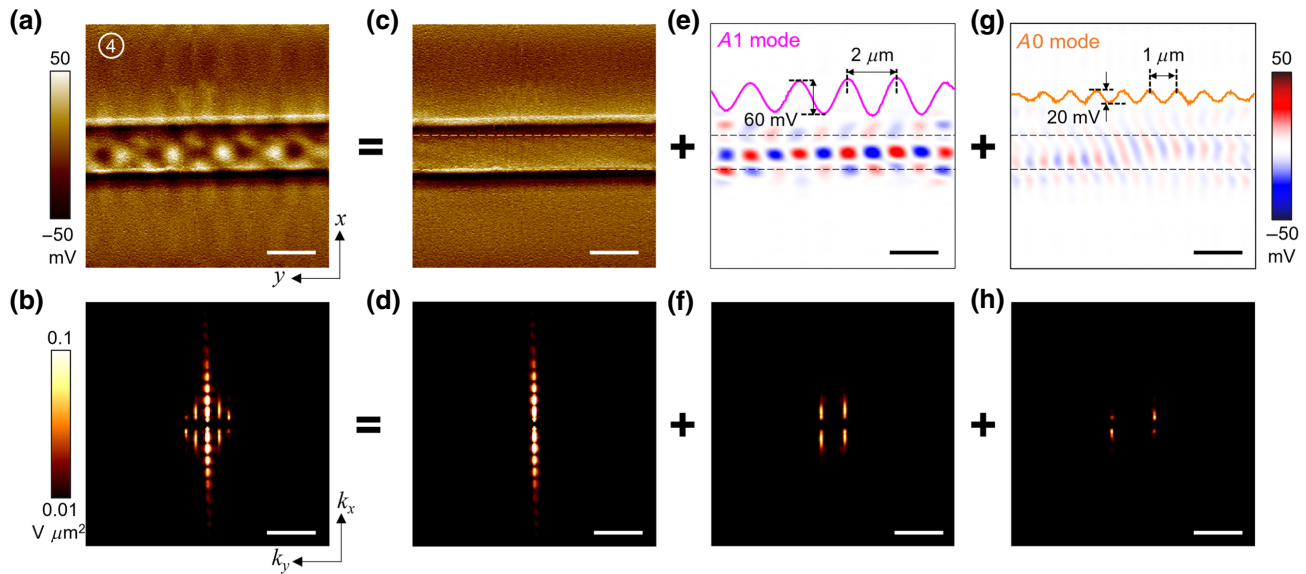


FIG. 4. (a) TMIM image and (b) its 2D FFT spectral image in box 4 in Fig. 3(b). (c) Filtered TMIM and (d) FFT images of the topographic artifact due to tranches on both sides of the waveguide. (e) Filtered TMIM and (f) FFT images associated with the *A*1 mode. (g) Filtered TMIM and (h) FFT images associated with the *A*0 mode. Insets of (e),(g) show line cuts through center of the images. Note that (a) is the superposition of (c),(e),(g) in the real space and (b) superposition of (d),(f),(h) in the *k*-space. Scale bars are 2 μm for real-space images and $2\pi \times 2 \mu\text{m}^{-1}$ for *k*-space FFT images.

of the surface potential is clearly observed. By taking FFT [Fig. 4(b)] of raw data, one can see that the TMIM results are a superposition of three distinct harmonic components. The fringelike pattern along the k_x direction in the FFT spectrum [Fig. 4(d)] corresponds to the double-slit feature in the TMIM image [Fig. 4(c)], which is from horizontal boundaries of the waveguide. Because of the finite size of the AFM tip, the waveguide appears to be slightly wider in the TMIM image than its actual width of 1 μm . Other than this topographic crosstalk, the most prominent FFT features are the four bright lines at $|k_y| = 2\pi \times 0.5 \mu\text{m}^{-1}$ [Fig. 4(f)]. The inverse FFT image in Fig. 4(e) reveals that they are associated with the *A*1 mode with out-of-phase motion between the center and boundary of the waveguide, as depicted in Fig. 2(c). Note that the signals outside the suspended nanobeam in Fig. 4(e) are due to both FFT filtering of the eigenmode profile

[Fig. 2(c)] and a topographic artifact when the tip plunges into the grooves on each side of the waveguide. Finally, the FFT image also displays weak but discernible features at $|k_y| = 2\pi \times 1 \mu\text{m}^{-1}$ [Fig. 4(h)]. The corresponding real-space image in Fig. 4(g) suggests that this is the *A*0 mode with in-phase particle motion across the width of the waveguide [Fig. 2(b)]. The line profiles through the center of Figs. 4(e) and 4(g) are plotted in the corresponding insets, showing $\lambda = 2$ and 1 μm for the two modes, respectively. By comparing the amplitudes of the two modes, it is obvious that the *A*1 mode is the dominant mode excited in the waveguide. In other words, the antisymmetric membrane mode in the parabolic coupler is mostly converted to the *A*1 mode in the waveguide, presumably due to mode conversion occurring near the tip of the parabolic coupler, where the wavefront is distorted from the planar wavefront from the IDT [Figs. 3(g)–3(j)]. This conversion is

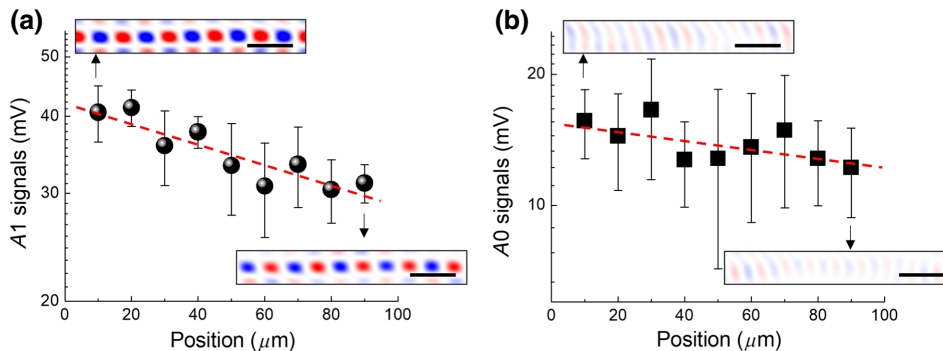


FIG. 5. TMIM signals of (a) *A*1 and (b) *A*0 modes along the 100- μm waveguide. Insets show the filtered TMIM images associated with *A*1 and *A*0 modes near the entrance and exit points of the waveguide. Red dashed lines are linear fits to semilogarithmic plots. All scale bars are 2 μm .

undesired for many applications where the $A0$ mode in the waveguide is preferred [26]. Therefore, a better design of the coupler will be needed and the TMIM measurement can provide critical insights.

The FFT filtering method described above allows us to remove topographic crosstalk from TMIM data and analyze oscillating amplitudes of individual waveguide modes. Figures 5(a) and 5(b) plot the TMIM signals of $A1$ and $A0$ modes through the 100- μm -long suspended waveguide, respectively. Representative FFT-filtered images are also shown near the entrance and exit points of the waveguide. For the primary $A1$ mode, the amplitude drops by a factor of about 1.5 over a length of 100 μm . The acoustic power loss is thus about 35 dB/mm, which is reasonable for the narrow waveguide. On the other hand, decay of the $A0$ mode is smaller, about 20 dB/mm [26], although the error bar is large due to the weak signals and distorted wave profiles.

IV. DISCUSSION

Quantitative analysis of the TMIM results reveals important information about the acoustic mode evolution in the suspended phononic circuit that cannot be obtained by two-port measurements. S_{21} data in Fig. 1(c), for instance, convolve piezoelectric and inverse piezoelectric transduction at the two IDTs, acoustic propagation in the two parabolic couplers, and mode conversion in and out of the waveguide. In contrast, TMIM imaging and FFT filtering allow us to focus on the waveguide modes and extract their acoustic loss in the narrow waveguide. The imaging method also reveals acoustic mode coupling between the parabolic horn and the waveguide. When the Lamb wave enters the waveguide, the TMIM peak-to-peak signal drops from about 100 mV on the coupler side [Fig. 3(g)] to about 60 mV in the waveguide [Fig. 4(e)]. Since the acoustic power is proportional to the square of the oscillation amplitude and the width of the free-standing film, we can calculate a power-coupling coefficient of about 20% by assuming a ratio of 2:1 in effective width near the entrance point. After propagation of 100 μm , the TMIM signal drops to about 40 mV at the end of the waveguide. Using the same coupling coefficient, one can estimate a TMIM signal of 10–15 mV when entering the left parabolic coupler, consistent with measured data in Fig. 3(k). From the measured S_{21} of about -40 dB, we obtain an electromechanical power conversion factor of 6–7% at the IDTs, which matches well with that of typical IDTs on AlN membranes [21,22,26]. As a result, the TMIM experiment provides a quantitative picture of various components in the phononic device down to the subwavelength scale.

Our work in visualizing GHz Lamb waves exemplifies the ability of TMIM to perform highly sensitive nanoscale acoustic imaging. From the calculated electromechanical

power-coupling efficiency, one can estimate the mechanical oscillation amplitude of 10 pm under an input power of 10 mW to the IDT (Appendix C). Furthermore, the good signal-to-noise ratio in the TMIM images indicates that the detection limit at a normal scan rate of 10 min per frame is in the order of 0.1 pm. This level of surface acoustic vibration is extremely challenging for scanning laser interferometry [33,34], stroboscopic x-ray imaging [38,39], and nonlinear acoustic force microscopy [44]. More importantly, at the operation frequency of about 3 GHz, the acoustic wavelength of 1–2 μm is too small for optics-based techniques, the spatial resolution of which is diffraction limited. The AFM-based TMIM experiment, on the other hand, can routinely resolve sub-100-nm features in acoustic imaging. For even higher frequencies in the 10-GHz regime, which is of critical importance for optomechanics and quantum acoustics, TMIM might be the only technique of choice to map out the acoustic patterns on complex device structures [46].

V. CONCLUSION

We report the fabrication of suspended AlN acoustic waveguides and the visualization of 3.44-GHz Lamb waves on such phononic devices. Combining finite-element modeling and transmission-mode microwave microscopy, we are able to identify the membrane and waveguide modes and quantitatively analyze acoustic coupling between the subwavelength waveguide and a pair of parabolic couplers. FFT filtering allows us to separate the contribution from the two eigenmodes of the waveguide and calculate their acoustic loss. Our work demonstrates the exquisite sensitivity and high resolution of the TMIM technique, which is expected to find future applications in electromechanics, optomechanics, and quantum science and engineering.

ACKNOWLEDGMENTS

The TMIM work is supported by NSF Division of Materials Research Grant No. DMR-2004536 and Welch Foundation Grant No. F-1814. Data analysis is partially supported by the NSF through the Center for Dynamics and Control of Materials, an NSF Materials Research Science and Engineering Center (MRSEC) under Cooperative Agreement No. DMR-1720595. The phononic waveguide work is supported by NSF Grants No. EFMA-1741656 and No. EFMA-1641109. Part of this work is conducted at the Washington Nanofabrication Facility/Molecular Analysis Facility, a National Nanotechnology Coordinated Infrastructure (NNCI) site at the University of Washington with partial support from the National Science Foundation via Grants No. NNCI-1542101 and No. NNCI-2025489.

APPENDIX A: FINITE-ELEMENT MODELING OF THE WAVEGUIDE MODES

Figure 6 shows the finite-element modeling result of our suspended AlN waveguide. Panels (a–c), (d–f), and (g–i) correspond to displacement profiles of the symmetric S_0 mode, antisymmetric A_0 mode, and antisymmetric A_1 mode, respectively.

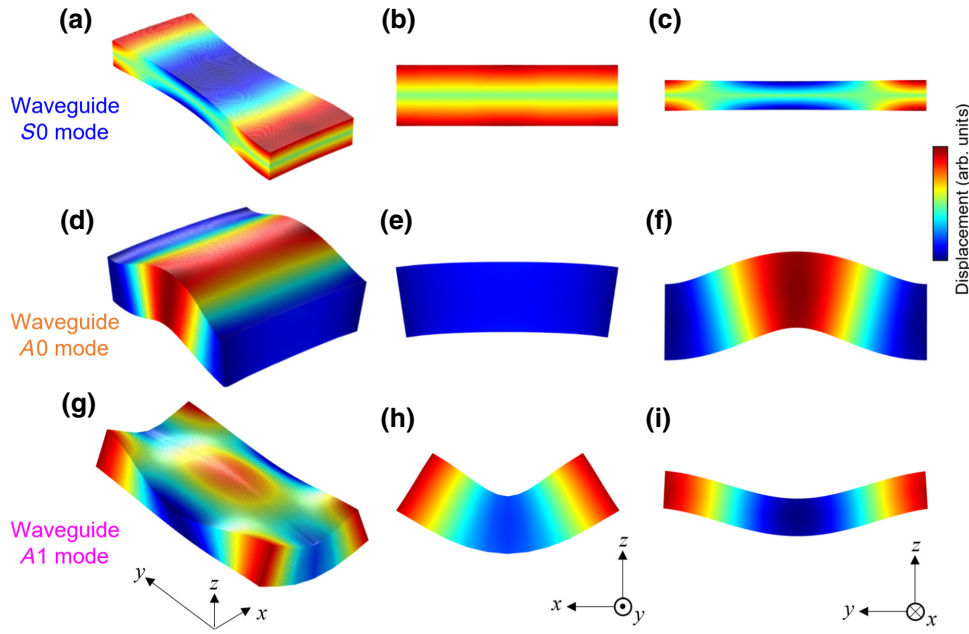


FIG. 6. Finite-element modeling results of (a)–(c) S_0 , (d)–(f) A_0 , and (g)–(i) A_1 modes of the suspended AlN waveguide (330 nm thick and 1 μm wide). Panels (a),(d),(g) are 3D views. Panels (b),(e),(h) are projections in the x - z plane. Panels (c),(f),(i) are projections in the y - z plane. Periodic boundary conditions are used for the x - z plane and free-moving boundary for the x - y and y - z planes.

APPENDIX B: AFM AND TMIM IMAGES IN A LARGE FIELD OF VIEW

Figure 7 shows the simultaneously acquired AFM and TMIM images of the AlN waveguide device in a large field of view. The I/Q mixer in the TMIM electronics generates two orthogonal output channels, as displayed in Figs. 7(b) and 7(c). The total TMIM signals, as plotted in Fig. 5, are vector sums of signals from the two channels. A plot of the TMIM-2 signal in Fig. 7(d) along the center of the waveguide shows the small decay of acoustic waves.

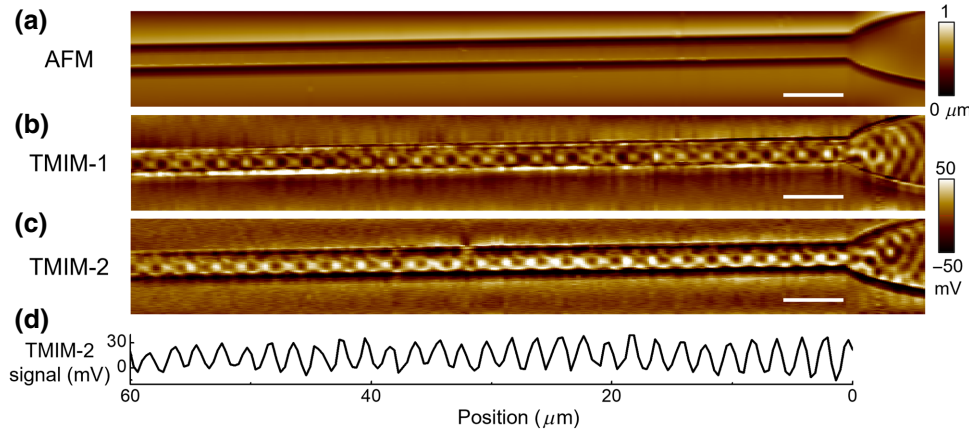


FIG. 7. (a) AFM, (b) TMIM-1, and (c) TMIM-2 images in a large field of view. Scale bars are 5 μm . (d) TMIM-2 signals along the center of the waveguide in (c).

APPENDIX C: FEM SIMULATION OF THE SURFACE DISPLACEMENTS AND ELECTRIC POTENTIAL

Figure 8 shows the numerically simulated out-of-plane and in-plane surface displacement fields and electric potential. The period of IDT is set to be $3 \mu\text{m}$. Each unit cell consists of 4 fingers with a spacing of 375 nm between adjacent fingers. The IDT is excited with 10 dBm input.

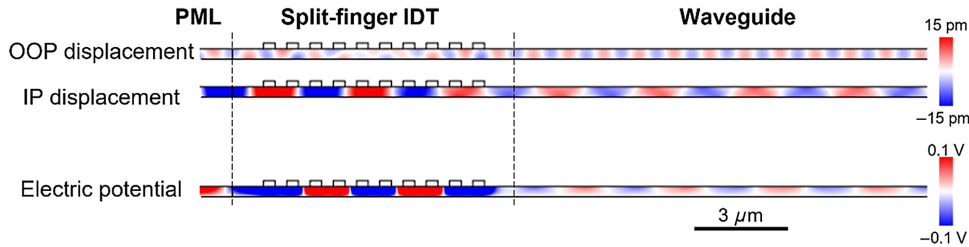


FIG. 8. Simulated displacement fields and electric potential on the suspended AlN membrane device under $\pm 1 \text{ V}$ excitation or about 10 mV input power at the split-finger IDT. Mechanical oscillation amplitude is in the order of 10 pm . Both out-of-plane and in-plane displacements contribute to the surface potential through different piezoelectric components (d_{33} and d_{31}) of the c -axis polycrystalline AlN membrane. OOP, out of plane; IP, in plane; PML, perfectly matching layer.

- [1] C. Campbell, *Surface Acoustic Wave Devices for Mobile and Wireless Communications* (Academic Press, San Diego, 1998). Applications of modern acoustics.
- [2] K.-Y. Hashimoto, *Surface Acoustic Wave Devices in Telecommunications: Modelling and Simulation* (Springer, Berlin, New York, 2000).
- [3] D. P. Morgan, *Surface Acoustic Wave Filters: with Applications to Electronic Communications and Signal Processing*, 2nd ed. (Academic Press, Amsterdam, London, 2007).
- [4] D. Ballantine Jr., R. M. White, S. J. Martin, A. J. Ricco, E. Zellers, G. Frye, and H. Wohltjen, *Acoustic Wave Sensors: Theory, Design and Physico-Chemical Applications* (Academic Press, San Diego, CA, 1997).
- [5] M. V. Gustafsson, T. Aref, A. F. Kockum, M. K. Ekstrom, G. Johansson, and P. Delsing, Propagating phonons coupled to an artificial atom, *Science* **346**, 207 (2014).
- [6] M. J. A. Schuetz, E. M. Kessler, G. Giedke, L. M. K. Vandersypen, M. D. Lukin, and J. I. Cirac, Universal quantum transducers based on surface acoustic waves, *Phys. Rev. X* **5**, 031031 (2015).
- [7] Y. Chu, P. Kharel, W. H. Renninger, L. D. Burkhardt, L. Frunzio, P. T. Rakich, and R. J. Schoelkopf, Quantum acoustics with superconducting qubits, *Science* **358**, 199 (2017).
- [8] A. Noguchi, R. Yamazaki, Y. Tabuchi, and Y. Nakamura, Qubit-Assisted Transduction for a Detection of Surface Acoustic Waves Near the Quantum Limit, *Phys. Rev. Lett.* **119**, 180505 (2017).
- [9] M. K. Ekström, T. Aref, J. Runeson, J. Björck, I. Boström, and P. Delsing, Surface acoustic wave unidirectional transducers for quantum applications, *Appl. Phys. Lett.* **110**, 073105 (2017).
- [10] B. A. Moores, L. R. Sletten, J. J. Viennot, and K. W. Lehnert, Cavity Quantum Acoustic Device in the Multimode Strong Coupling Regime, *Phys. Rev. Lett.* **120**, 227701 (2018).

- [11] E. R. MacQuarrie, T. A. Gosavi, N. R. Jungwirth, S. A. Bhave, and G. D. Fuchs, Mechanical Spin Control of Nitrogen-Vacancy Centers in Diamond, *Phys. Rev. Lett.* **111**, 227602 (2013).
- [12] P. Ovartchaiyapong, K. W. Lee, B. A. Myers, and A. C. Jayich, Dynamic strain-mediated coupling of a single diamond spin to a mechanical resonator, *Nat. Commun.* **5**, 4429 (2014).
- [13] D. A. Golter, T. Oo, M. Amezcua, K. A. Stewart, and H. Wang, Optomechanical Quantum Control of a Nitrogen-Vacancy Center in Diamond, *Phys. Rev. Lett.* **116**, 143602 (2016).
- [14] K. W. Lee, D. Lee, P. Ovartchaiyapong, J. Minguzzi, J. R. Maze, and A. C. B. Jayich, Strain Coupling of a Mechanical Resonator to a Single Quantum Emitter in Diamond, *Phys. Rev. App.* **6**, 034005 (2016).
- [15] S. Meesala, *et al.*, Strain engineering of the silicon-vacancy center in diamond, *Phys. Rev. B* **97**, 205444 (2018).
- [16] R. Manenti, M. J. Peterer, A. Nersisyan, E. B. Magnusson, A. Patterson, and P. J. Leek, Surface acoustic wave resonators in the quantum regime, *Phys. Rev. B* **93**, 041411(R) (2016).
- [17] E. B. Magnusson, B. H. Williams, R. Manenti, M. S. Nam, A. Nersisyan, M. J. Peterer, A. Ardavan, and P. J. Leek, Surface acoustic wave devices on bulk ZnO crystals at low temperature, *Appl. Phys. Lett.* **106**, 063509 (2015).
- [18] M. Mirhosseini, A. Sipahigil, M. Kalaei, and O. Painter, Superconducting qubit to optical photon transduction, *Nature* **588**, 599 (2020).
- [19] F. M. Mayor, W. Jiang, C. J. Sarabalis, T. P. McKenna, J. D. Witmer, and A. H. Safavi-Naeini, Physical Review Applied 15, Gigahertz Phononic Integrated Circuits on Thin-Film Lithium Niobate on Sapphire, *Phys. Rev. App.* **15**, 014039 (2021).
- [20] W. Fu, Z. Shen, Y. Xu, C. L. Zou, R. Cheng, X. Han, and H. X. Tang, Phononic integrated circuitry and

- spin-orbit interaction of phonons, *Nat. Commun.* **10**, 2743 (2019).
- [21] H. Li, Q. Liu, and M. Li, Electromechanical brillouin scattering in integrated planar photonics, *APL Photonics* **4**, 080802 (2019).
- [22] H. Li, S. A. Tadesse, Q. Liu, and M. Li, Nanophotonic cavity optomechanics with propagating acoustic waves at frequencies up to 12 GHz, *Optica* **2**, 826 (2015).
- [23] E. A. Kittlaus, H. Shin, and P. T. Rakich, Large brillouin amplification in silicon, *Nat. Photonics* **10**, 463 (2016).
- [24] H. Shin, W. Qiu, R. Jarecki, J. A. Cox, R. H. Olsson, 3rd, A. Starbuck, Z. Wang, and P. T. Rakich, Tailorable stimulated Brillouin scattering in nanoscale silicon waveguides, *Nat. Commun.* **4**, 1944 (2013).
- [25] A. H. Safavi-Naeini, D. Van Thourhout, R. Baets, and R. Van Laer, Controlling phonons and photons at the wavelength scale: Integrated photonics meets integrated phononics, *Optica* **6**, 213 (2019).
- [26] Q. Y. Liu, H. Li, and M. Li, Electromechanical Brillouin scattering in integrated optomechanical waveguides, *Optica* **6**, 778 (2019).
- [27] K. Yamanouchi and Y. Satoh, Ultra Low-insertion-loss surface acoustic wave filters using unidirectional interdigital transducers with grating SAW substrates, *Jpn. J. Appl. Phys.* **44**, 4532 (2005).
- [28] W. Jiang, C. J. Sarabalis, Y. D. Dahmani, R. N. Patel, F. M. Mayor, T. P. McKenna, R. Van Laer, and A. H. Safavi-Naeini, Efficient bidirectional piezo-optomechanical transduction between microwave and optical frequency, *Nat. Commun.* **11**, 1166 (2020).
- [29] X. Han, W. Fu, C. Zhong, C. L. Zou, Y. Xu, A. A. Sayem, M. Xu, S. Wang, R. Cheng, L. Jiang, and H. X. Tang, Cavity piezo-mechanics for superconducting-nanophotonic quantum interface, *Nat. Commun.* **11**, 3237 (2020).
- [30] M. S. Kushwaha, P. Halevi, L. Dobrzynski, and B. Djafari-Rouhani, Acoustic Band Structure of Periodic Elastic Composites, *Phys. Rev. Lett.* **71**, 2022 (1993).
- [31] A. Mahjoubfar, K. Goda, A. Ayazi, A. Fard, S. H. Kim, and B. Jalali, High-speed nanometer-resolved imaging vibrometer and velocimeter, *Appl. Phys. Lett.* **98**, 101107 (2011).
- [32] Y. Xu, W. Fu, C.-L. Zou, Z. Shen, and H. X. Tang, High quality factor surface fabry-perot cavity of acoustic waves, *Appl. Phys. Lett.* **112**, 073505 (2018).
- [33] Y. Sugawara, O. Wright, O. Matsuda, M. Takigahira, Y. Tanaka, S. Tamura, and V. Gusev, Watching Ripples on Crystals, *Phys. Rev. Lett.* **88**, 185504 (2002).
- [34] D. M. Profunser, O. B. Wright, and O. Matsuda, Imaging Ripples on Phononic Crystals Reveals Acoustic Band Structure and Bloch Harmonics, *Phys. Rev. Lett.* **97**, 055502 (2006).
- [35] K. Kokkonen and M. Kaivola, Scanning heterodyne laser interferometer for phase-sensitive absolute-amplitude measurements of surface vibrations, *Appl. Phys. Lett.* **92**, 063502 (2008).
- [36] K.-Y. Hashimoto, K. Kashiwa, N. Wu, T. Omori, M. Yamaguchi, O. Takano, S. Meguro, and K. Akahane, A laser probe based on a sagnac interferometer with fast mechanical scan for RF surface and bulk acoustic wave devices, *IEEE Trans. Ultrason. Ferroelectr. Freq. Control* **58**, 187 (2011).
- [37] Z. Shen, X. Han, C.-L. Zou, and H. X. Tang, Phase sensitive imaging of 10 GHz vibrations in an AlN microdisk resonator, *Rev. Sci. Instrum.* **88**, 123709 (2017).
- [38] R. Whatmore, P. Goddard, B. Tanner, and G. Clark, Direct imaging of travelling Rayleigh waves by stroboscopic X-ray topography, *Nature* **299**, 44 (1982).
- [39] E. Zolotoyabko, D. Shilo, W. Sauer, E. Pernot, and J. Baruchel, Visualization of 10 μm surface acoustic waves by stroboscopic x-ray topography, *Appl. Phys. Lett.* **73**, 2278 (1998).
- [40] D. Roshchupkin, T. Fournier, M. Brunel, O. Plotitsyna, and N. Sorokin, Scanning electron microscopy observation of excitation of the surface acoustic waves by the regular domain structures in the LiNbO₃ crystals, *Appl. Phys. Lett.* **60**, 2330 (1992).
- [41] D. Roshchupkin, M. Brunel, R. Tucoulou, E. Bigler, and N. Sorokin, Reflection of surface acoustic waves on domain walls in a LiNbO₃ crystal, *Appl. Phys. Lett.* **64**, 164 (1994).
- [42] W. Rohrbeck, E. Chilla, H.-J. Fröhlich, and J. Riedel, Detection of surface acoustic waves by scanning tunneling microscopy, *Appl. Phys. A* **52**, 344 (1991).
- [43] E. Chilla, W. Rohrbeck, H. J. Fröhlich, R. Koch, and K. Rieder, Probing of surface acoustic wave fields by a novel scanning tunneling microscopy technique: Effects of topography, *Appl. Phys. Lett.* **61**, 3107 (1992).
- [44] T. Hesjedal, Surface acoustic wave-assisted scanning probe microscopy—a summary, *Rep. Prog. Phys.* **73**, 016102 (2009).
- [45] L. Zheng, D. Wu, X. Wu, and K. Lai, Visualization of Surface-Acoustic-Wave Potential by Transmission-Mode Microwave Impedance Microscopy, *Phys. Rev. Appl.* **9**, 061002 (2018).
- [46] L. Zheng, L. Shao, M. Loncar, and K. Lai, Imaging acoustic waves by microwave microscopy: Microwave impedance microscopy for visualizing gigahertz acoustic waves, *IEEE Microw. Mag.* **21**, 60 (2020).
- [47] I. Yao, in *1980 Ultrasonics Symposium* (IEEE, 1980), pp. 37.
- [48] M. M. de Lima Jr and P. V. Santos, Modulation of photonic structures by surface acoustic waves, *Rep. Prog. Phys.* **68**, 1639 (2005).